
Article:
Levin, I., Keeble, D.S., Cibin, G. et al. (5 more authors) (2019) Nanoscale polar heterogeneities and branching Bi-displacement directions in K0.5Bi0.5TiO3. Chemistry of Materials, 31 (7). pp. 2450-2458. ISSN 0897-4756

https://doi.org/10.1021/acs.chemmater.8b05187

Nanoscale polar heterogeneities and branching Bi-displacement directions in $K_{0.5}Bi_{0.5}TiO_3$

Igor Levin[1*], Dean S. Keeble[2], Giannantonio Cibin[2], Helen Y. Playford[3], Maksim Eremenko[1], Victor Krayzman[1], William J. Laws[1], Ian M. Reaney[4]

[1] Materials Measurement Science Division
National Institute of Standards and Technology, Gaithersburg MD 208988 USA

[2] Diamond Light Source, Ltd., Didcot, OX, UK

[3] ISIS Facility, Science and Technology Facilities Council, Didcot, OX UK

[4]Department of Materials Science and Engineering, University of Sheffield, Sheffield UK

[*]igor.levin@nist.gov

Abstract

$K_{0.5}Bi_{0.5}TiO_3$ (KBT) – one of the few perovskite-like ferroelectric compounds with room-temperature tetragonal symmetry – differs from other members of this family ($BaTiO_3$ and $PbTiO_3$) by the presence of a disordered mixture of K and Bi on cuboctahedral sites. This disorder is expected to affect local atomic displacements and their response to an applied electric field. We have derived nanoscale atomistic models of KBT by refining atomic coordinates to simultaneously fit neutron/X-ray total-scattering and extended X-ray absorption fine-structure data. Both Bi and Ti ions were found to be offset relative to their respective oxygen cages in the high-temperature cubic phase; in contrast, the coordination environment of K remained relatively undistorted. In the cubic structure, Bi displacements prefer the ⟨100⟩ directions and the probability-density distribution of Bi features six well-separated sites; a similar preference exists for the much smaller Ti displacements although the split sites for Ti could not be resolved. The cation displacements are correlated, yielding polar nanoregions, while on average the structure appears as cubic. The cubic↔tetragonal phase transition involves both order-disorder and displacive mechanisms. A qualitative change in the form of the Bi probability-density distribution occurs in the tetragonal phase on cooling to room temperature because Bi displacements "branch off" to ⟨111⟩ directions. This change, which preserves the average symmetry, is accompanied by the development of nanoscale polar heterogeneities that exhibit significant deviations of their polarization vectors from the average polar axis.

Introduction

Bismuth-based transition-metal oxides with perovskite-like (ABO_3) structures exhibit dielectric, ferroelectric, and ion-conduction properties of interest for several device applications [1-5]. In these systems, Bi atoms, which occupy relatively large [BiO_{12}] cuboctahedral cages formed by vertex-sharing [BO_6] octahedra, are stabilized by forming shorter, covalent bonds with one or several oxygen atoms. Such short Bi-O bonds are typically enabled by octahedral rotations and/or off-center Bi displacements. The magnitudes of Bi displacements and the associated electric dipoles are maximized if octahedral rotations are suppressed. In these cases, concerted Bi off-centering is expected to yield a proportionately large spontaneous polarization. However, most Bi-based perovskites of practical interest are either compounds, such as $Na_{½}Bi_{½}TiO_3$ or $K_{½}Bi_{½}TiO_3$, which contain a disordered mixture of Bi and other species on the cuboctahedral sites, or complex multicomponent solid solutions (e.g., $BaTiO_3$-$BiScO_3$ or $PbTiO_3$-$BiFeO_3$). In both cases, this chemical disorder hinders the cooperative alignment of Bi displacements.

Thus far, relatively few detailed studies of local structure in Bi-based compounds have been reported [6-9]. From these works, Bi appears to be offset preferentially along specific crystallographic directions, which include ⟨100⟩ and ⟨111⟩. In $Na_{½}Bi_{½}TiO_3$, an end member in several well-studied ferroelectric systems, the preferential direction reportedly varies from ⟨100⟩ in the high-temperature tetragonal phase to ⟨111⟩ in the lower-temperature rhombohedral polymorph [8]; in the intermediate temperature range, both types of displacements coexist [8] within a complex hierarchical structure that features rhombohedral-like pseudosymmetry [10]. The ⟨100⟩ and ⟨111⟩ displacements also coexist in the pseudo-cubic $BaTiO_3$-$BiScO_3$ solid solutions, creating a 14-site probability density distribution for the Bi atoms [11]. These solid solutions, which exhibit dielectric properties of interest for high energy-density capacitor applications [3], reveal no macroscopic signs of symmetry-lowering down to 15 K, while the relative magnitudes of displacements along the two directions vary with temperature. No conclusive relationships between the local chemistry and the displacement preferences have been established.

$K_{½}Bi_{½}TiO_3$ (KBT) is one of the few known perovskite ferroelectrics with room-temperature tetragonal *P4mm* symmetry (along with the classical $BaTiO_3$ and $PbTiO_3$). As such, it has attracted attention as a component in piezoelectric solid solutions, several of which yield technologically relevant properties [11-12]. Despite multiple studies [13-21], the details of the KBT structure and the exact nature of its ferroelectric cubic↔tetragonal phase transition remain uncertain. Analysis of the literature reveals two different results. In several publications [13, 18], KBT was observed to exhibit a room-temperature c/a ratio of ≈1.01. This tetragonal phase remains stable up to 270 °C, above which it transforms first to a pseudo-cubic phase and then, at T=400 °C, to a "genuinely" cubic structure. Other publications [14-15] report the tetragonal phase to have a larger c/a ratio of ≈1.015 to ≈1.02 at room temperature, a significantly higher Curie temperature of ≈360 °C, and a sharp transition to the cubic phase, all of which suggest a more homogeneous distribution of Bi and K compared to the first type of results. Presumably, these discrepancies are related to small variations in the K/Bi ratio caused by using hygroscopic K_2CO_3 as a starting material, and/or volatility of both K and Bi at synthesis temperatures. According to a recent study [16] dedicated to the effects of composition on the structure and properties of KBT, the c/a ratio varies weakly (around ≈1.02) with deviations from stoichiometric K/Ti and Bi/Ti ratios; one exception is the $K_{0.49}Bi_{0.5}TiO_3$, for which c/a≈1.01. Thus, KBT compositions with smaller tetragonal distortions are most likely K-deficient.

The distinct ionic radii and charges of K^+ (ionic radius 1.64 Å) and Bi^{3+} (1.36 Å) cations, with the latter containing a stereochemically active "lone" pair of electrons [22], are expected to yield local structural distortions that will influence the dielectric and ferroelectric properties. Recently, the local structure in KBT (of the 1st type, with a broad tetragonal-cubic transition) has been studied using X-ray atomic pair-distribution function (PDF) combined with first-principles calculations [18-19]. The main conclusions of this work included the existence of unspecified "local polar regions" in the tetragonal ferroelectric polymorph and the order-disorder nature of the tetragonal-cubic phase transition; the latter phenomenon has been inferred from the temperature-invariant Bi-Ti distance distribution and interpreted in terms of polar Ti displacements. The differences in the distortions of the Bi and K coordination environments have been noted but with little discussion of the Bi displacements, which are expected to define the dielectric and ferroelectric responses of KBT. These displacements acquire large magnitudes as indicated by the published Bi-O distance distributions. Likewise, the thermal invariance of instantaneous interatomic distances per se provides no definitive indication of the phase-transition mechanism.

Therefore, in the present work we revisited the local structure of KBT and obtained detailed insights into the local atomic displacements and their correlations via a combined use of variable-temperature neutron and X-ray total-scattering data and extended X-ray absorption fine structure (EXAFS). Our results clarified the hypotheses proposed in previous works [18-19], while revealing several hitherto unsuspected phenomena. Specifically, the paraelectric cubic and the ferroelectric tetragonal polymorphs of KBT are both shown to contain nanoscale polar heterogeneities associated with spatially correlated Bi and Ti displacements. The cubic↔tetragonal phase transition appears to have a mixed character with order/disorder and displacive components present. The probability density distribution of Bi exhibits a split-site distribution, which in the tetragonal phase, on cooling, transforms from a 6-site to a 10-site form without affecting the average symmetry.

Experimental

The KBT samples were processed using conventional solid-state synthesis starting from powders of K_2CO_3 (A.R.), Bi_2O_3 (99.999 %), and TiO_2 (<10 ppm P_2O_5) as raw materials. Prior to weighing, K_2CO_3 was dried in an oven at 180 °C. The raw powders were mixed under acetone using an agate mortar and pestle. After drying, the mixtures were ball-milled in isopropanol in a planetary mill with yttria-stabilized zirconia cylinders as a grinding media. The dried powders were calcined at 850 °C. After subsequent ball milling, the powders were pressed into pellets and heated in air at 1000 °C for 5 h twice with intermediate grinding. Laboratory X-ray diffraction (XRD) with Cu $K\alpha_1$ radiation was used to confirm phase purity. Variable-temperature neutron and X-ray total scattering data were collected using Polaris (ISIS facility, UK) and I-15-A (Diamond Light Source, UK) beamlines, respectively. For neutron-scattering measurements, the sample powder was loaded in a vanadium can. X-ray-scattering measurements were performed using an incident beam energy of 76.7 keV with a Perkin-Elmer 2D detector positioned at 235-mm downstream from the sample. The sample was loaded in a 0.4-mm quartz capillary and spun during measurements. The instrumental resolution functions of both the neutron and X-ray instrument configurations were determined by measuring NIST's Si SRM 640c. The neutron data were processed using GUDRUN [23] to obtain a total scattering function and its corresponding pair-distribution function, $G(r)$. The X-ray 2D data were reduced in the DAWN [24] software package and then converted to the total-scattering function and $G(r)$ using PDFGetX3 [25]. Extended X-ray absorption fine structure (EXAFS) measurements were performed for the Bi L_3- and K K-edges at the B18 beamline of the Diamond Light

Source, with the data collected in transmission and fluorescence modes, respectively. A 9-element Ge detector was used for the fluorescence measurements. The samples were thin pellets obtained from mixtures of the KBT powder with appropriate amounts of boron nitride. Bi EXAFS was measured as a function of temperature, whereas data collection for the K EXAFS was limited to ambient conditions because of the relatively low energy for the potassium *K* edge, which makes it difficult to obtain a sufficiently high signal through the furnace window as required for measurements at elevated temperatures. The EXAFS data were reduced using the Athena software package; preliminary fitting of these data using a parameterized structural model was performed in Artemis [26] to determine the energy shifts, E_0, and the amplitude reduction factors, S_0^2, for both the Bi and K datasets. The scattering amplitudes and phases were calculated using FEFF8 [27]. TEM studies were conducted in a conventional instrument operated at 200 kV. Samples for TEM were prepared either using mechanical polishing followed by ion thinning at T=-100 °C until perforation.

Atomistic structure refinements were performed in the development version of the RMCProfile software [28-30]. The structure was modeled using atomic configurations which contained $32 \times 32 \times 32$ unit cells (163,840 atoms), sampling interatomic distances up to 6 nm. A random distribution of K and Bi was assumed because electron diffraction patterns of KBT contained no diffuse-scattering features that could be attributed to short-range chemical order. The atomic coordinates were varied according to a Reverse Monte Carlo (RMC) algorithm to simultaneously fit both X-ray and neutron total-scattering functions, their corresponding real-space Fourier transforms (which represent atomic pair distribution functions), and the neutron Bragg profile. The Bi and K EXAFS datasets were also included in the fit to improve chemical resolution; the implementation of EXAFS fitting in RMCProfile has been detailed in [29; see also Supplemental Information]. For the EXAFS data, E_0 and S_0^2 were kept fixed at their values obtained from the analysis in Artemis. The calculated EXAFS signal included contributions from photoelectron single-scattering paths for the nearest-neighbor A-O (A=K or Bi), A-Ti, A-A, and next-nearest-neighbor A-O and A-A coordination shells. For the K EXAFS, multiple scattering along the -K-O-K- atomic chains were also included; for the Bi EXAFS the effects of this multiple scattering was determined to be negligible. Atomistic models resulting from RMC refinements using total-scattering and EXAFS data represent structural snapshots. The reciprocal- and real-space forms of the neutron and X-ray scattering data were corrected for instrument resolution as described in [30]; accurate resolution corrections are critical for the determination of nanoscale displacement correlations. The weights assigned to the individual datasets were adjusted automatically during fits according to an algorithm that employs a statistical analysis to ensure that each residual term decreases over time to a small preset value.

Results and Discussion

Tetragonal phase

At room temperature, the Bragg peaks of KBT could all be accounted for by a tetragonal structure with a *c*/*a* ratio of ≈1.019. Fig. 1a displays a temperature dependence of *d*-spacings for the 112 and 121 tetragonal reflections. On heating, an abrupt transition to the cubic structure is observed around 360 °C, with the two reflections merging into a single peak. The width of this peak (i.e. cubic 112) continues to decrease upon heating up to ≈420 °C (Fig. 1b), suggesting the existence of a pseudo-cubic state between 360 °C and 420 °C. Above 420 °C, the structure is presumably cubic.

Fig. 2 presents variable-temperature X-ray PDFs (Fig. 2a) and selected partial PDFs (Fig. 2b) recovered from the RMC refinements. The X-ray PDF, which is dominated by distances involving the heavy Bi atoms, reveals the presence of short ≈2.2 Å Bi-O bonds that are typical for Bi-O coordination in perovskites and point to strong Bi off-centering (Fig. 2a). Such short Bi-O bond lengths are also confirmed by the Bi EXAFS data, consistent with previous reports [6]. In contrast, the K EXAFS indicates a weakly distorted K coordination with an average K-O distance of ≈2.8 Å. The tetragonal *P4mm* model provides a satisfactory fit to the X-ray PDF except for r<10 Å, as can be expected from the strongly dissimilar distortions around Bi and K. The distance dependence of the c/a ratio obtained by box-car fitting of the X-ray PDF using this model was less pronounced than that reported previously [18]; the discrepancy can be attributed to a more homogenous nature of the present samples as manifested in the relatively abrupt phase transition.

Multiple-technique RMC fitting resulted in close agreement between the experimental and calculated signals for all the datasets (Fig. 3). The quality of the PDF fits is maintained over the entire r-ranges. Partial PDFs calculated from the refined atomic coordinates confirm significant Bi off-centering, which contrasts with the relatively undistorted [KO_{12}] coordination (Fig. 2b). Consistent with previous reports, the distribution of the Bi-O bond lengths (Fig. 2b) changes little between the tetragonal and cubic structures.

Fig. 4 summarizes probability density distributions (PDD) of Bi determined from the refined atomic coordinates for several representative temperatures. The room-temperature PDD acquires a square pyramidal shape with the main maximum displaced by ≈0.5 Å from the ideal centrosymmetric position along the c-axis (Fig. 4a). Systematic slicing of this PDD perpendicular to the c-axis reveals the nine subsidiary maxima (shown schematically in Fig. 5), with the four of them, having a higher density, offset approximately along the ⟨111⟩ directions and the remaining five displaced along the ⟨100⟩ directions other than [001]. (Fig. 4a, Fig. 5a). Fig. 6 displays a stereographic-map of the Bi displacements relative to the ideal cubic position. In addition to the dominant shifts along the tetragonal c-axis (i.e., the cubic [001] direction), a clear preference for the ⟨111⟩ directions is evident. Thus, at room temperature, the Bi atoms in the tetragonal phase are distributed (with unequal probability) among the ten split sites (Fig. 5).

The PDDs of K, Ti, and O display no visible anomalies. As typical for perovskites, O atoms exhibit larger displacements normal to the Ti-O bonds. Magnitudes of atomic displacements depend on the local K/Bi chemistry as illustrated in Fig. 7. The local Ti off-centering within the oxygen octahedra increases with an increasing number of Bi atoms around Ti (Fig. 7a); this effect can be ascribed to the oxygen-mediated correlations among the Bi and Ti displacements so that the off-centering of Bi promotes that of Ti. Similar trends have been reported previously for several other perovskite solid solutions that contain off-centered species on both octahedral and cuboctahedral sites [31, 32].

Fig. 8 shows displacement fields for the [010]-columns of Bi atoms projected onto the (010) plane. The arrows describe the displacements of the column projections from their positions in the cubic structure. For the tetragonal phase (Fig. 8a), the z-axis coincides with the [001] direction. As evident in Fig. 8a, the z-axis displacement-components for all the columns are positively correlated, consistent with a tetragonal structure. However, the off-axis displacements also exhibit strong positive correlations, yielding nanoscale regions (like the one encircled in the figure) with significant deviations of their net displacement vectors from the average tetragonal axis. Similar effects are observed for Ti. (Fig. 8b presents a displacement field for the cubic structure and will be discussed in the next section).

In three dimensions, the spatial extent of correlations among the off-axis Bi displacements, like those that occur along the ⟨111⟩ directions, can be assessed by considering histograms (Fig. 9) that describe distributions of distances between the Bi atoms displaced along a particular ⟨111⟩ direction. Fig. 9a compares such histograms for the refined configuration "as is" and for the same configuration but with the Bi-displacement vectors shuffled randomly over the Bi positions. Such shuffling preserves PDDs but eliminates displacement correlations, thereby providing a reference configuration with random displacements; for brevity, hereafter, we will refer to configurations modified using this procedure as "shuffled". As detailed in the figure caption, the total numbers of atoms displaced along a given ⟨111⟩ direction in the as-refined and shuffled cases are the same; however, the number of such atoms separated by shorter distances (a portion of the histograms displayed in the figure) is significantly larger in the former. This confirms a pronounced clustering of the ⟨111⟩ displacements over a length scale encompassing multiple unit cells.

We performed a similar analysis for the unit-cell polarization vectors which were calculated from the refined atomic coordinates/displacements and the Born effective charges adopted from literature (Fig. 10). In this case, the histograms described the distributions of distances between the unit cells which have their polarization vectors aligned with a given ⟨111⟩ direction (Fig. 10a). A comparison with the shuffled configuration provides a strong evidence for the presence of polar clusters with the ⟨111⟩-like polarization directions. The local polarization magnitude (the total, not the *z*-component like suggested in [18]) decreases as the sampling volume increases (Fig. 10b). This type of dependence is expected for any structural snapshot because of thermal motion; however, in KBT the trend is enhanced by large Bi displacements. The presence of nanoscale polar heterogeneities results in a slower decay of polarization as compared to a random case.

An overall effective correlation length for atomic displacements can be estimated from the difference between PDFs calculated for the refined and shuffled configurations. For random displacements, this difference is expected to be flat over the entire distance range, whereas if correlations are present, it will decay from a maximum at shorter *r* to a base level at longer distances. In the present case, the X-ray PDF emphasizes Bi displacements, whereas its neutron analog reflects contributions from all the species. Clearly, both difference curves (Fig. 11a) reveal strong correlations with the characteristic length, *L* (defined in the figure) in the range of to 2 nm to 3 nm; the effect is most pronounced for Bi. This behavior is consistent with the inferences from Fig. 8a and 9a.

Thus, at room temperature, the tetragonal phase exhibits significant spatially extended fluctuations of polarization because Bi displacements from the average position are correlated and branch off to directions that form large angles with the tetragonal axis. At 300 °C, the net Bi off-centering is reduced relative to its value at room temperature with a concurrent increase in the probability density at the off-axis ⟨100⟩ maxima of the Bi PDD (Fig. 4b); that is, heating promotes the disorder of Bi among the split sites. Given the strong correlations among the Bi and Ti displacements, a similar behavior is expected for Ti; however, its split sites remain unresolvable likely because of the relatively small values of the Ti displacements. In contrast to room temperature, at 300 °C no detectable concentration of the probability density is observed for the ⟨111⟩ Bi displacements. Therefore, the preferred displacement directions change from ⟨100⟩ to ⟨100⟩ + ⟨111⟩ between 300 °C and 25 °C. We call this type of change "*branching*". Branching displacements modify a form of the corresponding PDD without affecting average symmetry as exemplified by the tetragonal KBT (Fig. 4). An isosymmetric branching transition increases the number

of split sites within a PDD, in contrast to transitions associated with ordering of displacements, such as encountered in $AgNbO_3$ [33].

The coexistence of ⟨111⟩ and ⟨100⟩ Bi displacements in the distorted phase resembles the case of NBT [7], albeit with the reversed relative dominance of the two types of directions. The factors that determine the preference for Bi to be displaced along specific directions are still unclear. In NBT, cation displacements are coupled to octahedral rotations which evolve with varying temperature and can affect the displacement directions; however, in KBT, the rotations are absent. One factor common to both compounds is a disordered mixture of the Bi and alkaline ions. In NBT, no conclusive relationship has been established between the local chemistry and the displacement directions. We looked for such correlations in KBT but likewise could not find any. Conceivably, the displacement direction depends on a combined effect of a local K/Bi ratio and a specific configuration of nearest-neighbor K and Bi atoms around a given Bi; however, this type of analysis has not been implemented in the present study.

Cubic phase and tetragonal↔cubic phase transition

In the cubic phase, both Bi and Ti species remain off-centered as evident from the variable-temperature X-ray PDF (Fig. 2a) and Bi EXAFS. At both 400°C and 500 °C, the Bi displacements exhibit a clear preference for the ⟨100⟩ directions (Fig. 4b, c; Fig. 5b, c, Fig. 6b, c), yielding a split 6-site PDD with a minimum density at the central position. No signs of preferential ⟨111⟩ displacements can be observed. However, as temperature is reduced from 500 °C to 400 °C, a relative probability density for the displacement directions other than ⟨100⟩ appears to increase, as can be inferred from a more rounded shape of the PDD. The magnitude of the Bi displacements grows with the increasing number of K atoms around Bi (Fig. 7b), which is consistent with a larger effective size of the $[BiO_{12}]$ cages for the K-rich regions.

The evolution of the Bi PDDs with decreasing temperature, which displays redistribution of the probability density over the split ⟨100⟩ sites (Fig. 5) is a signature of the order/disorder character of the tetragonal↔cubic transition. However, the separation of the split sites also varies both across the phase transition and within the tetragonal phase, which suggests that the phase transition has a mixed character with both order/disorder and displacive components present.

Projections of the refined configurations reveal pronounced spatial clustering of the parallel Bi (and Ti) displacements, which persists even at 500 °C (Fig. 8b). The effective correlation length for the atomic displacements assessed, as described above, from the difference between the PDFs calculated for the refined and "shuffled" configurations, is shorter relative to that at room temperature but remains in the 1.5 nm to 2 nm range (Fig. 11c-f). Extensive tests were performed to ensure that the presence of such extended correlations at high temperatures is not an artifact introduced by inaccurate instrument-resolution corrections. These tests included fits with the *r*-ranges for the PDF data limited to r_{max}=30 Å (for such shorter distances, the resolution effects remain minimal) and fits over the full distance ranges but with the instrument-resolution parameters varied by ±20 %. In all the cases, qualitatively similar polar clusters were obtained suggesting that the observed nanoscale correlations are real.

Thus, the KBT structure is pseudocubic even above 420 °C, with the polar nanoregions (PNRs) which can be viewed as representing the six crystallographic variants of the tetragonal phase. These PNRs explain the relaxor dielectric response recently reported for the cubic phase of KBT; the Burns temperature has been determined as ≈560 °C but the authors suggested that polar nanoregions in KBT may exist at even higher temperatures. While the number of temperatures sampled in the present study is insufficient to

follow changes in the correlation length across the cubic↔tetragonal phase transition, we conjecture that that this length increases substantially below 400 °C, yielding a measurable broadening of the diffraction peaks (Fig. 1b) because of a larger coherence length for lattice distortions.

Summary

In KBT, both Bi and Ti cations are off-centered relative to their respective oxygen cages in the high temperature cubic phase, with each of these species distributed statistically over the six sites offset along the ⟨100⟩ directions. On cooling, at the cubic↔tetragonal transition, partial ordering of the Bi and Ti displacements occurs, as manifested in the increased occupancy of one of the six split sites, which results in a macroscopic spontaneous polarization along the corresponding ⟨100⟩ direction that becomes the tetragonal *c*-axis. A branching transition ⟨100⟩ → ⟨100⟩ + ⟨111⟩ for the preferred directions of Bi displacements occurs in the tetragonal phase, which is reflected in a change from a 6-site to a 10-site Bi probability-density distribution. The off-center cation displacements are strongly correlated even in the cubic phase at temperatures as high as 500 °C, yielding polar nanoregions ≈2 nm in size. The correlation length increases markedly in the tetragonal phase, yielding macroscopic domains. However, the ⟨111⟩ Bi displacements in the tetragonal structure are still correlated locally, thereby yielding extended regions that have their polarization vectors directed at a large angle to the average tetragonal axis. Recent dielectric measurements on KBT reveal no relaxation effects at room temperature, which suggests that these polar heterogeneities can be effectively frozen. The factors that favor one type of Bi displacement directions over the other remain unclear. Given the commonalities in the preferred directions identified for several technologically-relevant Bi-based systems, computational studies targeting these preferences could be warranted to provide the knowledge necessary for tuning of Bi displacements, thereby modifying the resulting dielectric and ferroelectric properties.

Acknowledgements

Experiments at the ISIS Pulsed Neutron and Muon Source were supported by a beamtime allocation from the UK Science and Technology Facility Council (data DOI 10.5286/ISIS.E.87770362). We thank Diamond Light Source for access to beamlines I15-1 (Proposals EE16168 and EE19240) and B18 (Proposal SP16460).

Supporting Information

A description of the EXAFS-fitting procedure.

Figure Captions:

Fig. 1: (a) Temperature dependence of the *d*-spacings for the 112 and 121 tetragonal reflections in the neutron diffraction patterns. On heating, the reflections merge at ≈360 °C, which signifies a phase transition to the cubic polymorph. (b) Temperature dependence of the full-width-at-half-maximum for the cubic 112 peak. The error bars reflect a single standard deviation as determined by the fitting procedure; for the *d*-spacings, these errors are within the symbol size.

Fig. 2: (a) Low-*r* portions of the X-ray PDFs at a series of temperatures (indicated using different colors) between 25 °C and 500 °C. Higher temperatures can be recognized by broader Bi-Ti peaks. The short Bi-O bond lengths of ≈2.2 Å persist up to at least 500 °C. (b) Low-*r* portions of the selected partial PDFs at 25 °C (thick lines) and 500 °C (thin lines) as calculated from the refined atomic coordinates. (red) Ti-O; (green) Bi-O; (blue) K-O.

Fig. 3: (a-d) Experimental (red) and calculated (blue) signals for KBT at 25° C: (a, b) neutron total-scattering and pair-distribution functions, respectively; (c, d) X-ray total-scattering and pair-distribution functions, respectively. The residual curves are shown in green. (e, f) Experimental (dashed) and calculated (solid) signals of the EXAFS Fourier Transforms (FT) for Bi and K, respectively. The magnitude, real, and imaginary parts of the FT are indicated using red, green, and blues colors, respectively. The *k*-space EXAFS data have been multiplied by *k* prior to the FT. The *k*-ranges used in the FT are from 2.78 $Å^{-1}$ to 10.65 $Å^{-1}$ for K and from 3.13 $Å^{-1}$to 11.04 $Å^{-1}$ for Bi; in both cases, the *r*-space fitting ranges was from 1 Å to 3.5 Å, which encompass the first three coordination spheres around the A-cations. All the calculated signals correspond to the same atomistic model. Note: The presence of at least some discrepancies between the experimental and calculated signals is expected given the inevitable systematic errors in each dataset plus those introduced by the assumptions (e.g., data weighing) involved in data fitting.

Fig. 4: Probability density distributions (PDDs) of Bi at several temperatures (indicated along the bottom) in the tetragonal (a, b) and cubic (c, d) phase fields. (top row) {*xz*) projections of the PDDs. For the tetragonal phase, the *c*-axis is along *z*. (rows A-D) Projections of the {*xy*} slices of the respective PDDs. The slices, each 0.25 Å thick, are labelled according to their *z*-positions as indicated in the top-row. In the B-slices, the circles indicate the maxima which are displaced along the ⟨100⟩ directions, whereas the arrows point to the four maxima offset approximately along ⟨111⟩. In the tetragonal phase, the total number of Bi atoms displaced within the cones, each having a 20° semi-angle and centered on one the 4 preferred ⟨111⟩ directions, is about half of those displaced within a similar cone centered on the tetragonal [001] direction and twice the total number of Bi atoms displaced along the 4 ⟨100⟩ directions perpendicular to the tetragonal axis.

Fig. 5: A schematic illustration of the evolution of the split-site Bi PDD with increasing temperature. (a) and (b) correspond to the tetragonal phase, whereas (c) represents the cubic polymorph. Darker shades correspond to a higher probability.

Fig. 6: Stereographic-projection maps of the Bi-displacement directions at several representative temperatures as indicated in the figure. The displacements were determined relative to the ideal

cubic positions. At room temperature, in addition to the dominant Bi shifts along the tetragonal c-axis (i.e., the cubic [001] direction), a clear preference for the ⟨111⟩ directions is observed.

Fig. 7: (a) The Ti-off-centering (T=25 °C) and (b) the displacements of Bi off the ideal cubic positions (T=500 °C) as a function of the Bi content in the local (Bi, K) coordination sphere. The trend for the Ti off-centering shown in (a) is preserved in the cubic phase.

Fig. 8: Displacement fields for projections of the [010] Bi columns onto the (010) planes for the tetragonal (a) and cubic structures (b) at 25 °C and 500 °C, respectively. The axes indicate the lateral scale in Å. The arrows indicate the displacements of the column projections relative to their ideal average positions in the cubic structure. For the tetragonal case, the *c*-axis is along *z*. In (a), an example area with strong positive correlations of the off-axis displacements is encircled. In (b) circles also outline areas with the strong positive correlations of displacements.

Fig. 9: (a) Histograms of distance distributions *only* for the Bi atoms that are displaced within a cone (20° semi-angle) centered on one of the four ⟨111⟩ directions preferred by the Bi displacements at 25 °C. The histograms were first calculated for each ⟨111⟩ direction separately and then averaged together; the error bars represent two standard deviations that correspond to this averaging. The red and blue colors correspond to the as-refined and shuffled configurations. (b) Similar histograms for the cubic phase at 500 °C but with the Bi-displacement cones centered on the ⟨100⟩ directions. In both cases, the plots display only the short-distance portions of the histograms which were calculated out to 16 lattice parameters. The total numbers of atoms that contribute to the histograms over the entire distance range are the same for as refined and shuffled configurations. However, the numbers of these atoms separated by short distances are significantly larger for the former. For both temperatures, histograms reveal the presence of extended spatial correlations among the corresponding Bi displacements.

Fig. 10: (a) Histograms of distance distributions *only* for unit cells that have their electrical polarization vectors fall within a cone (20° semi-angle) centered on one of the four ⟨111⟩ directions preferred by the Bi displacements at 25 °C. The red and blue colors correspond to the as-refined and shuffled configurations. The histograms were first calculated for each ⟨111⟩ direction separately and then averaged together; the error bars represent two standard deviations that correspond to this averaging. (b) The polarization modulus calculated for the refined (red) and shuffled (blue) configurations at 25 °C as a function of a sampling volume, $N \times N \times N$ unit cells. For N=1, this modulus value corresponds to an average of the moduli for the unit-cell polarization vectors. For N>1, each value represents an average of the polarization moduli calculated for a volume of $N \times N \times N$ unit cells while sliding this sampling box over the configuration as in the boxcar method. The polarization averages to its macroscopic value at a length scale of five to six unit cells, which corresponds to ≈2 nm, consistent with the correlation length for the atomic displacements identified from Figs 9 and 10. The decay of the polarization modulus with N for the refined configuration is considerably slower than that for the shuffled case without displacement correlations.

Fig. 11: X-ray (a, c, e) and neutron (b, d, f) PDFs calculated for the KBT configurations as refined and after random shuffling of the atomic displacements over the positions of the corresponding species. The

behavior of the difference signals (green) reflects the presence of displacement correlations (see the main text) that extend to at least 2 nm. (a, b) 25 °C, (c, d) 400 °C, (e, f) 500 °C.

References:

1. T. Takenaka, K. Maruyama, K. Sakata, $(Bi_{½}Na_{½})TiO_3$-$BaTiO_3$ system for lead-free piezoelectric ceramics, Jpn. J. Appl. Phys., 30 (1) 9B, 2236-2239 (1991)
2. T. R. Shrout, S. J. Zhang, Lead-free piezoelectric ceramics: Alternatives for PZT, J. Electroceram., 19 (1) 113-126 (2007)
3. J. Rodel, W. Jo, K. T. P. Seifert, E-M. Anton, T. Granzow, D. Damjanovic, Perspective on the development of lead-free piezoceramics, J. Am. Ceram. Soc., 92 (6) 1153-1177 (2009)
4. M. A. Beuerlein, N. Kumar, T-M. Usher, H. J. Brown-Shaklee, N. Raengthon, I. M. Reaney, D. P. Cann, J. L. Jones, G. L. Brennecka, Current understanding of structure-property relationships in $BaTiO_3$-$Bi(M)O_3$ dielectrics, J. Am. Ceram. Soc., 99 (9) 2849-2870 (2016)
5. M. Li, M. J. Pietrowski, R. A. De Souza, H. Zhang, I. M. Reaney, S. N. Cook, J. A. Kilner, D. C. Sinclair, A family of oxide ion conductors based on the ferroelectric perovskite $Na_{0.5}Bi_{0.5}TiO_3$, Nat. Mater., 13 (1) 31-36 (2013)
6. V. A. Shuvaeva, D. Zekria, A. M. Glazer, Q. Jiang, S. M. Weber, P. Bhattacharya, P. A. Thomas, Local structure of the lead-free relaxor ferroelectric $(K_xNa_{1-x})_{0.5}Bi_{0.5}TiO_3$, Phys. Rev., B., 71, 174114 (2005)
7. D. S. Keeble, E. R. Barney, D. A. Keen, M. G. Tucker, J. Kreisel, P. A. Thomas. Bifurcated polarization rotation in bismuth-based piezoelectrics. Adv. Funct. Mater., 23, 185-190 (2013)
8. E. Aksel, J. Forrester, J. Nino, K. Page, D. P. Shoemaker, J. L. Jones, Local atomic structure deviation from average structure of $Na_{0.5}Bi_{0.5}TiO_3$: Combined X-ray and neutron total scattering, Phys. Rev. B., 103113 (2013)
9. I. Levin, V. Krayzman, J. C. Woicik, F. Bridges, G. E. Sterbinsky, T-M. Usher, J. L. Jones, D. Torrejon, Local structure in $BaTiO_3$-$BiScO_3$ dipole glasses, Phys. Rev. B., 93, 104106 (2016)
10. I. Levin and I. M. Reaney, Nano and mesoscale structure of $Na_{½}Bi_{½}TiO_3$: a TEM perspective, Adv. Funct. Mater., 22 (16), 3445-3452 (2012)
11. O. Elkechai, M. Manier, J. P. Mercurio, $Na_{0.5}Bi_{0.5}TiO_3$-$K_{0.5}Bi_{0.5}TiO_3$ (NBT-KBT) system: a structural and electrical study, Phys. Stat. Sol. (a), 157, 499-506 (1996)
12. 2. A. Khesro, D. Wang, F. Hussain, D. C. Sinclair, A. Feteira, I. M. Reaney, Temperature stable and fatigue resistant lead-free ceramics for actuators, Appl. Phys. Lett., 109 142907 (2016)
13. V. V Ivanova, A. G. Kapyshev, Y. N. Venevtsev, and G. S. Zhdanov, X-ray determination of the symmetry of elementary cells of the ferroelectric materials $(K_{0.5}Bi_{0.5})$ TiO_3 and $(Na_{0.5}Bi_{0.5})$ TiO_3 and of high-temperature phase transitions in (K0. 5Bi0. 5) TiO3, Izv. Akad. Nauk SSSR, vol. 26, pp. 354–356, 1962
14. 3. M. Otonicar, S. D. Skapin, B. Jancar, R. Ubic, D. Suvorov, Analysis of the phase transition and the domain structure in $K_{0.5}Bi_{0.5}TiO_3$ perovskite ceramics by in situ XRD and TEM., J. Am. Ceram. Soc., 93 [12] 4168-4173 (2010)
15. Y. Pu, P. Gao, T. Wu, X. Liu, Z. Dong, Dielectric and piezoelectric properties of $Bi_{0.5}K_{0.5}TiO_3$-$BaNb_2O_6$ lead-free piezoelectric ceramics, J. Elect. Mater., 44 (1) 332-340 (2015)
16. L. Li, M. Li, I. M. Reaney, D. C. Sinclair. Mixed ionic-electronic conduction in $K_{½}Bi_{½}TiO_3$, J. Mater. Chem. C., 5, 6300-6310 (2017)
17. P. V. B. Rao and T. B. Sankaram. Impedance spectroscopy studies of $K_{0.5}Bi_{0.5}TiO_3$, J. Electroceram., 25 (1), 60-69 (2010)

18. B. Jiang, T. Grande, S. M. Selbach, Local structure of disordered $Bi_{0.5}K_{0.5}TiO_3$ investigated by pair distribution function analysis and first principles calculations., Chem. Mater., 29 (10) 4244-4252 (2017)
19. B. Jiang, T. M. Raeder, D-Y. Lin, T. Grande, S. M. Selbach, Structural disorder and Coherence across the phase transitions of lead-free piezoelectric $Bi_{½}K_{½}TiO_3$, Chem. Mater., 30 (8) 2631-2640 (2018)
20. M. K. Niranjan, P. K. Kumari, K. Banerjee, S. Asthana, Randomly arranged cation-ordered regions in lead-free relaxor ferroelectric $K_{½}Bi_{½}TiO_3$: Prediction from first-principles study, J. Appl. Phys., 123, 244106 (2018)
21. M. Hagiwara, Y. Ehara, N. Novak, N. H. Khansur, A. Ayrikyan, K. G. Webber, S. Fujihara, Relaxor-ferroelectric crossover in $(Bi_{½}K_{½})TiO_3$: Origin of the spontaneous phase transition and the effect of an applied external field., Phys. Rev. B., 96, 014103 (2017)
22. R. Seshadri and N. A. Hill, Visualizing the Role of Bi 6s "Lone Pairs" in the Off-Center Distortion in Ferromagnetic $BiMnO_3$, Chem. Mater., 13, 2892-2899 (2001)
23. A. K. Sope. GUDRUN: Routines to Reducing Total Scattering Data. https://www.isis.stfc.ac.uk/Pages/Gudrun.aspx (accessed March 4, 2019)
24. M. Basham, J. Filik, M. T. Wharmby, P. C. Y. Chang, B. El Kassaby, M. Gerring, J. Aishima, K. Levik, B. C. A. Pulford, I. Sikharulidze, D. Sneddon, M. Webber, S. S. Dhesi, F. Maccherozzi, O. Svensson, S. Brockhauser, G. Na´rayc A. W. Ashtona, Data Analysis WorkbeNch (DAWN), J. Synch. Rad. 22, 853–858 (2015)
25. P. Juhás and T. Davis, C. L. Farrow, S. J. L. Billinge, PDFgetX3: A rapid and highly automatable program for processing powder diffraction data into total scattering pair distribution functions, J. *Appl. Cryst.* **46**, 560-566 (2013)
26. B. Ravel and M. Newville, *ATHENA*, *ARTEMIS*, *HEPHAESTUS*: data analysis for X-ray absorption spectroscopy using *IFEFFIT*. J. Synchrotron Rad. 12, 537--541 (2005).
27. J. J. Rehr, J. J. Kas, M. P. Prange, A. P. Sorini, Y. Takimoto, F. D. Vila, Ab initio theory and calculations of X-ray spectra*,* Comptes Rendus Physique 10 (6) 548-559 (2009)
28. M. G. Tucker, M. T. Dove, D. A. Keen, Application of the Reverse Monte Carlo method to crystalline materials, 34 (5), 630-638 (2001)
29. V. Krayzman, I. Levin, J. C. Woicik, Th. Proffen, T. A. Vanderah, M. G. Tucker, A combined fit of total scattering and extended X-ray absorption fine structure data for local-structure determination in crystalline materials, *J. Appl. Cryst.* 42, 867-877 (2009)
30. M. Eremenko, V. Krayzman, A. Gagin, I. Levin, Advancing Reverse Monte Carlo refinements to the nanoscale, J. Appl. Cryst., 50 (6) 1561-1570 (2017)
31. I. Levin, V. Krayzman, J. C. Woicik, Local-structure origins of the sustained Curie temperature in $(Ba,Ca)TiO_3$ ferroelectrics, Appl. Phys. Lett., 102, 162906 (2013)
32. I. Levin, V. Krayzman, G. Cibin, M. G. Tucker, M. Eremenko, K. Chapman, R. L. Paul, Coupling of emergent octahedral rotations to polarization in $(K,Na)NbO_3$ ferroelectrics, Sci. Rep., 7, 15620 (2017)
33. I. Levin, V. Krayzman, J. C. Woicik, J. Karapetrova, M. G. Tucker, I. M. Reaney, Structural Changes underlying the diffuse dielectric response in AgNbO3, Phys. Rev. B., 79, 104113 (2009)

TOC figure:

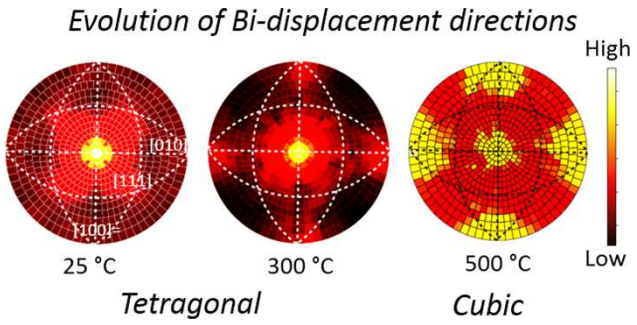
Evolution of Bi-displacement directions
High
Low
[010]
[111]
[100]
25 °C
300 °C
500 °C
Tetragonal
Cubic

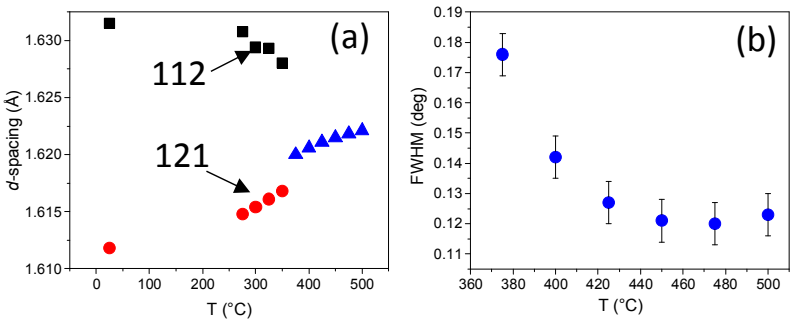

Fig. 1

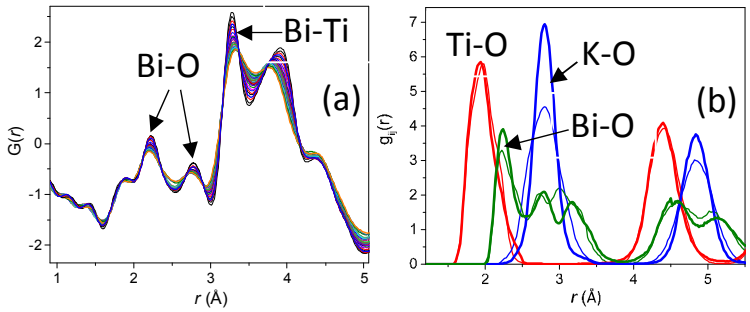

Fig. 2

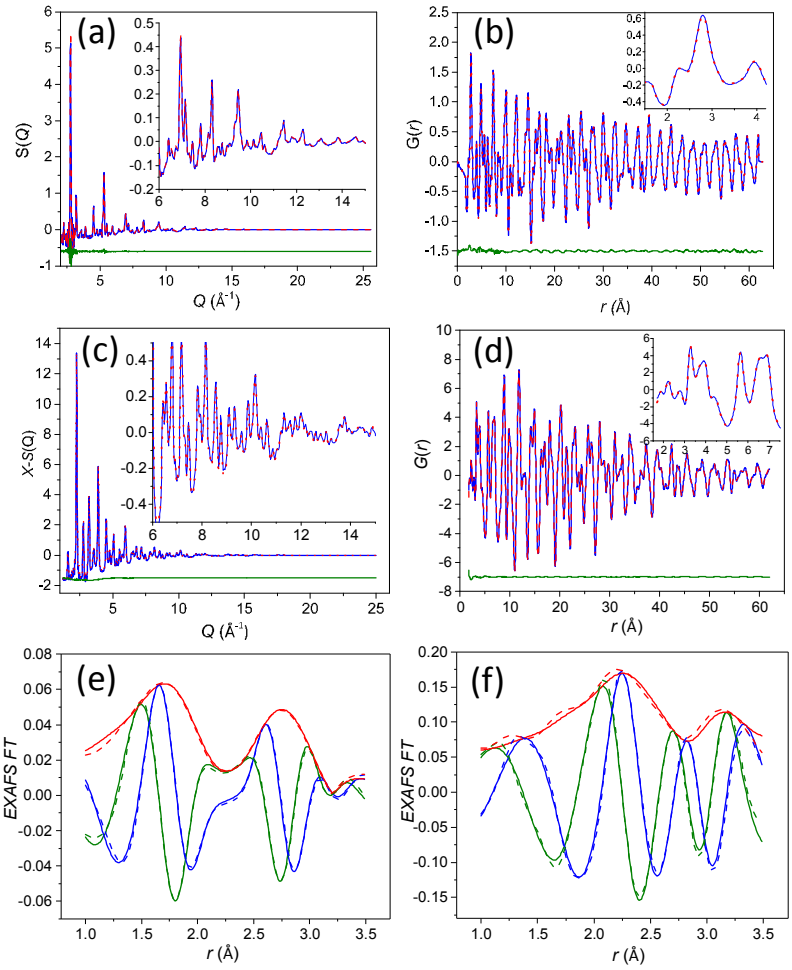

Fig. 3

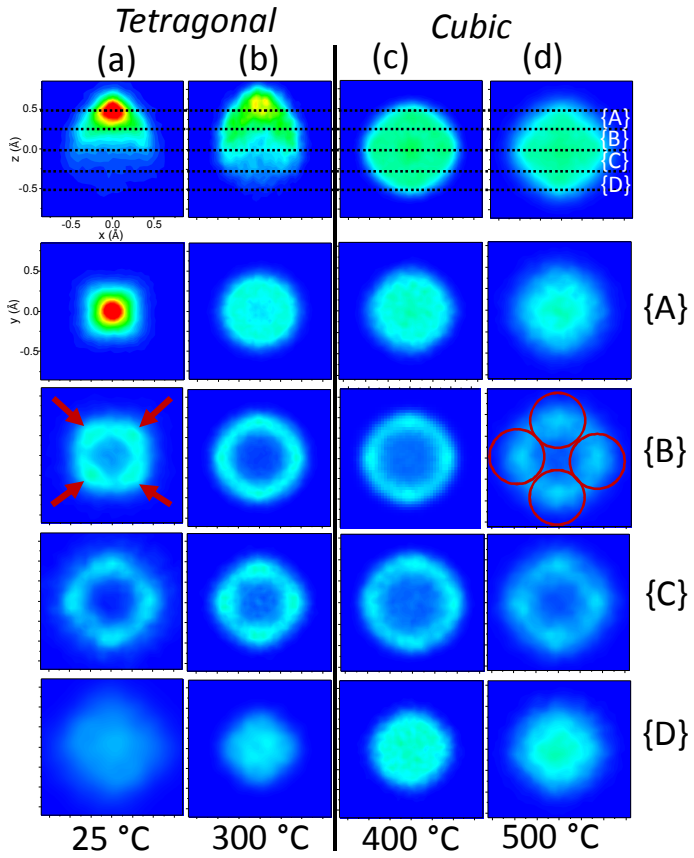
Tetragonal
Cubic
(a)
(b)
(c)
(d)
{A}
{B}
{C}
{D}
z (Å)
x (Å)
y (Å)
0.5
0.0
-0.5
25 °C
300 °C
400 °C
500 °C

Fig. 4

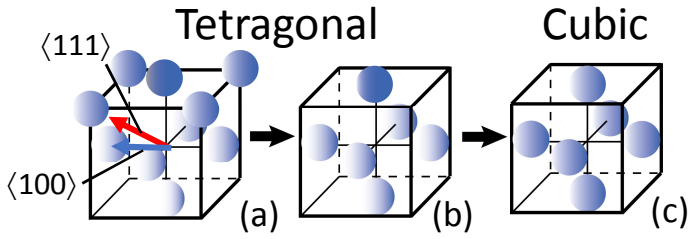

Fig. 5

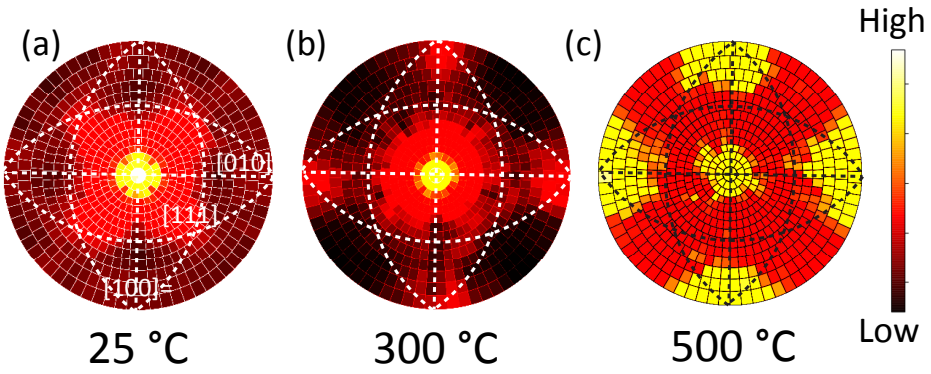

Fig. 6

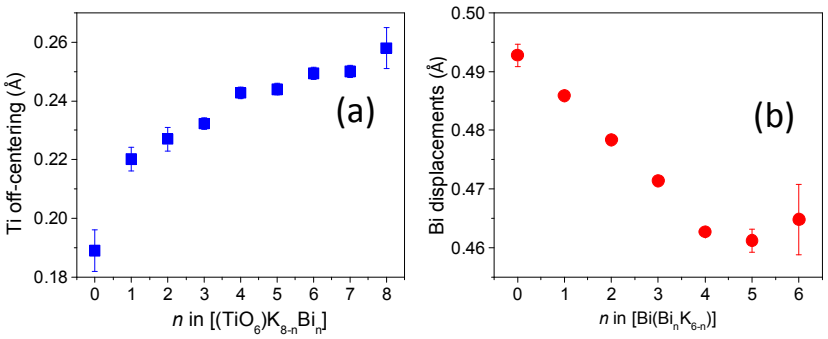
Ti off-centering (Å)
0.18
0.20
0.22
0.24
0.26
0
1
2
3
4
5
6
7
8
n in [(TiO6)K8-nBin]
(a)
Bi displacements (Å)
0.46
0.47
0.48
0.49
0.50
0
1
2
3
4
5
6
n in [Bi(BinK6-n)]
(b)

Fig. 7

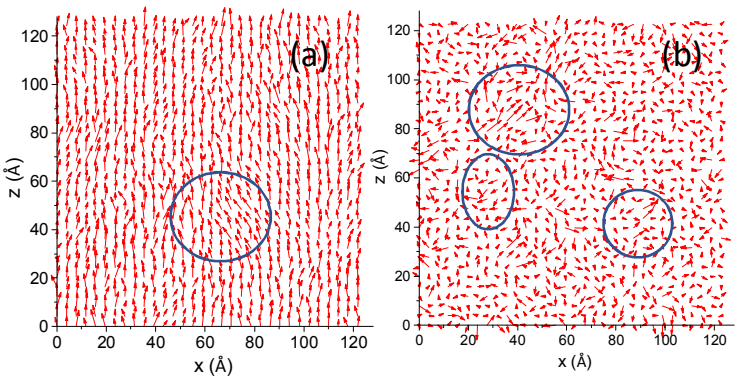

Fig. 8

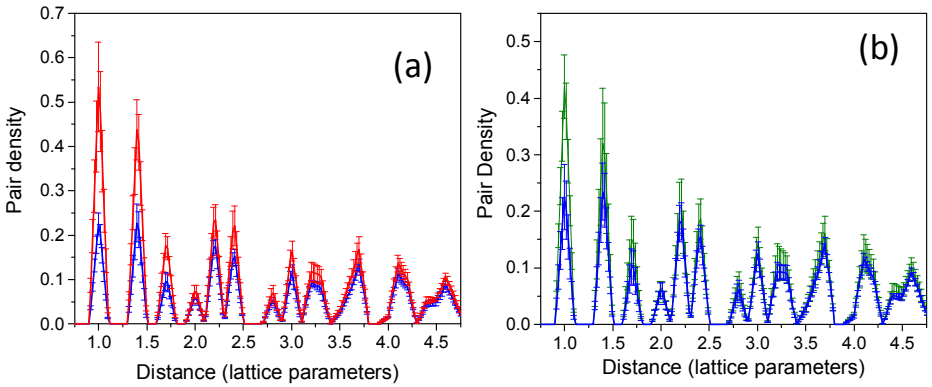
(a)
Pair density
Distance (lattice parameters)
(b)
Pair Density
Distance (lattice parameters)

Fig. 9

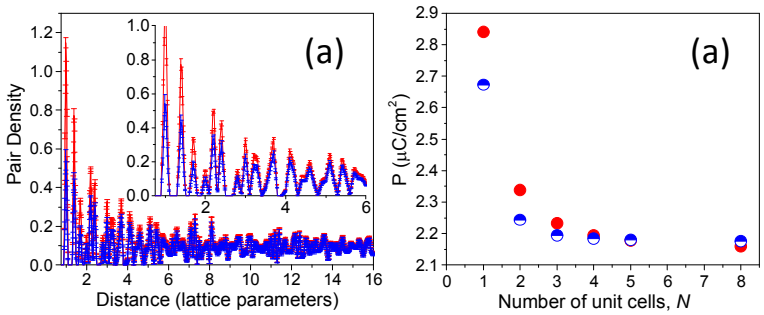
(a)
Pair Density
Distance (lattice parameters)
(a)
P (μC/cm²)
Number of unit cells, N

Fig. 10

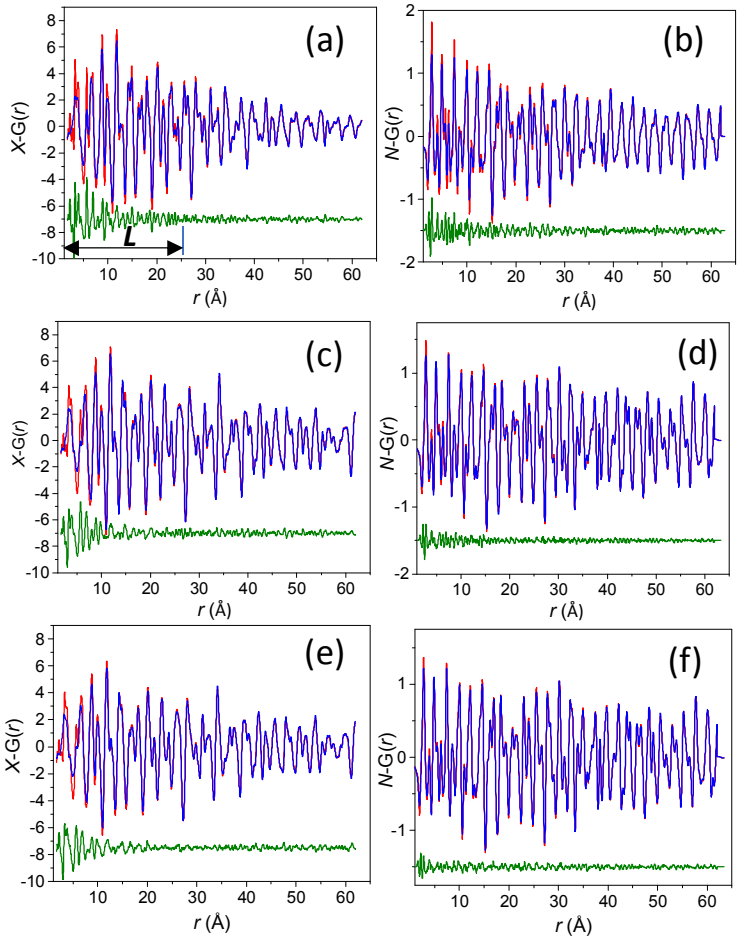

Fig. 11